

## Low-dimensional electronic state at the surface of a transparent conductive oxide

Muntaser Naamneh <sup>1,2,5</sup>, Eduardo B. Guedes<sup>2,5</sup>, Abhinav Prakash <sup>3</sup>, Henrique M. Cardoso<sup>4</sup>, Ming Shi <sup>2</sup>, Nicholas C. Plumb <sup>2</sup>, Walber H. Brito<sup>4</sup>, Bharat Jalan <sup>3</sup> & Milan Radović <sup>2</sup>

Materials that blend physical properties that are usually mutually exclusive could facilitate devices with novel functionalities. For example, the doped perovskite alkaline earth stannates BaSnO<sub>3</sub> and SrSnO<sub>3</sub> show the intriguing combination of high light transparency and high electrical conductivity. Understanding such emergent physics requires deep insight into the materials' electronic structures. Moreover, the band structure at the surfaces of those materials can deviate significantly from their bulk counterparts, thereby unlocking novel physical phenomena. Employing angle-resolved photoemission spectroscopy and ab initio calculations, we reveal the existence of a 2-dimensional metallic state at the SnO<sub>2</sub>-terminated surface of 1% La-doped BaSnO<sub>3</sub> thin films. The observed surface state is characterized by a distinct carrier density and a lower effective mass compared to the bulk conduction band, of about 0.12m<sub>e</sub>. These particular surface state properties place BaSnO<sub>3</sub> among the materials suitable for engineering highly conductive transition metal oxide heterostructures.

<sup>1</sup>Department of Physics, Ben-Gurion University of the Negev, Beer-Sheva 84105, Israel. <sup>2</sup>Photon Science Division, Paul Scherrer Institut, CH-5232 Villigen, Switzerland. <sup>3</sup>Department of Chemical Engineering and Materials Science, University of Minnesota, 421 Washington Ave., Minneapolis, MN 55455, USA. <sup>4</sup>Departamento de Física, Universidade Federal de Minas Gerais, C.P. 702, 30123-970 Belo Horizonte, Minas Gerais, Brazil. <sup>5</sup>These authors contributed equally: Muntaser Naamneh, Eduardo B. Guedes. ✉email: [mnaamneh@bgu.ac.il](mailto:mnaamneh@bgu.ac.il); [bjalan@umn.edu](mailto:bjalan@umn.edu); [milan.radovic@psi.ch](mailto:milan.radovic@psi.ch)

Over the last years, there has been a surge of interest in transparent conducting oxides (TCOs), which combine weak optical absorption with high electrical conductivity. This combination is possible when the bandgap remains wide (over 3 eV) while high doping is attained without affecting electron mobility, or in systems with a small bandgap but enhanced effective mass due to strong electron–electron interactions<sup>1</sup>. Perovskite alkaline earth stannates, such as BaSnO<sub>3</sub> (BSO) and SrSnO<sub>3</sub> (SSO), fulfill the requirements of the first and thus are promising candidates for realizing novel optoelectrical devices. In particular, BSO crystals with wide band gaps (~3.0–4.0 eV) have shown unusually high room temperature electron mobility of over 100 cm<sup>2</sup> V<sup>-1</sup> s<sup>-1</sup> (see ref. 2), while doped bulk BSO reaches mobility of 320 cm<sup>2</sup> V<sup>-1</sup> s<sup>-1</sup> (see ref. 3). Therefore, BSO demonstrates a realistic potential to replace traditional transparent conductive oxides, such as indium-based systems<sup>4</sup>, in optoelectronic technology. Furthermore, both BSO and SSO in thin film form show further improvement in light transparency, electrical conductivity<sup>5,6</sup>, and electron mobility compared to the bulk compounds, which is generally attributed to a low electron-effective mass in the range of 0.2–0.4 *m<sub>e</sub>*<sup>7–11</sup>. Significant theoretical and experimental efforts<sup>12–14</sup> have been made to understand these unique electronic properties. Band structure calculations based on density functional theory (DFT) found a low effective mass for the conducting state of bulk BSO<sup>11</sup>, which was attributed to a substantial reduction in the electron–phonon scattering rate.

Perovskite oxides generally exhibit the emergence of novel phenomena at surfaces and interfaces, manifesting tremendous potential for technological applications<sup>15,16</sup>. Indeed, it was suggested that stannates could host an interfacial electron gas since they experience polar interfaces band bending near the surface<sup>17</sup>. Kim et al. reported that LaInO<sub>3</sub>/(Ba,La)SnO<sub>3</sub> heterostructure shows enhancement of the conductance, suggesting that a 2-dimensional electron gas (2DEG) has been created at the interface<sup>6,18</sup>. Moreover, Feng et al. recently reported that 2DEG is generated at the interface between a thick BSO film and a thin LaAlO<sub>3</sub> capping layer<sup>19</sup> by the creation of oxygen vacancies. This result suggests that the 2DEG in BSO heterostructures is in some respects analogous to the one found in the LaAlO<sub>3</sub>/SrTiO<sub>3</sub> (LAO/STO) system, which is likewise a transparent conducting system<sup>20</sup>. Numerous insights into the electronic structure of the LAO/STO system have been obtained from ARPES studies of a 2DEG found on the bare STO surface<sup>21–23</sup>. Investigating the surface structure of BSO using angle-resolved photoemission spectroscopy should likewise be beneficial for understanding the properties exhibited by BSO-based heterostructures.

In this article, we report the investigation of BSO's surface electronic properties using a combination of angle-resolved photoemission spectroscopy (ARPES) on La-doped BaSnO<sub>3</sub> (LBSO) films and ab initio calculations. Our spectroscopy measurements demonstrate the existence of a two-dimensional (2D) state at the surface of LBSO thin films with distinct properties from the bulk. Comparing the experimental data with the calculated band structure for BSO in both bulk and slab forms, we find that the observed 2D state resides on the SnO<sub>2</sub>-terminated surface and features a significantly smaller effective mass than found in the bulk bands.

## Results and discussion

For this study, 30-nm-thick LBSO films were grown by hybrid molecular beam epitaxy (MBE) on Nb-doped STO (001) substrates. Figure 1a displays the X-ray diffraction pattern of an LBSO film. The out-of-plane lattice parameter of 4.140 ± 0.002 Å reveals that the studied LBSO film is mostly relaxed. A slightly higher out-of-plane lattice parameter compared to bulk LBSO is

due to the small residual biaxial strain in the film. Fringes around the (002) X-ray diffraction (XRD) peak of LBSO (Fig. 1a) are due to the finite film thickness and indicative of a smooth surface (see Supplementary Note 1 for more details). Figure 1b shows the reflection high-energy electron diffraction (RHEED) pattern of an as-grown sample (measured at the University of Minnesota). The sample's RHEED pattern after transport to the SIS beamline at the Swiss Light Source (Fig. 1c) was still well-defined, verifying the preservation of the surface's crystallinity. However, a relatively high background visible in the RHEED data indicated some surface contamination, and therefore we performed high-temperature annealing at 600 °C in 1.0 × 10<sup>-4</sup> mbar of O<sub>2</sub>. This procedure resulted in a significant improvement of the surface quality, as evidenced both by RHEED and low-energy electron diffraction (LEED) in Fig. 1d, e, respectively (see Supplementary Note 2 for more details). The RHEED pattern (Fig. 1d) exhibits a weak sign of surface reconstruction, which might be related to the  $\sqrt{2} \times \sqrt{2} R45^\circ$  reconstruction reported to occur after annealing up to 600–700 °C in ultrahigh vacuum<sup>13</sup>. The samples were then transferred in situ (pressure better than 5.0 × 10<sup>-10</sup> mbar) to the main experimental chamber, where the measured LEED pattern and ARPES data showed a 1 × 1-ordered surface.

ARPES is a powerful tool to directly determine the electronic band structures of materials and hence also the dimensionalities of their electronic states. In Fig. 2, we present the electronic band structure obtained from the LBSO films. The *k<sub>z</sub>* momentum is perpendicular to the sample surface and thus orthogonal to the *k<sub>x</sub>* and *k<sub>y</sub>* momenta, which lie on the surface plane along the (100) and (010) cubic axes, respectively. By varying the incoming photon energy from 20 to 145 eV, we measured band dispersions along *k<sub>x</sub>* at various *k<sub>z</sub>* values. Figure 2a displays the deep valence band structure along cuts parallel to  $\Gamma$ -X passing through the different *k<sub>z</sub>* values marked by white curves in Fig. 2b. To better visualize the bands, the spectra have been processed using the 2D curvature method<sup>24</sup>.

In Fig. 2a, we also compare the measured band structure to linearized quasiparticle self-consistent GW (LQSGW) calculations for bulk BSO using the experimental lattice constant of *a* = 4.14 Å (see Supplementary Note 3 for more details). For each spectrum image, we overlay the data with the calculated band structures at the corresponding *k<sub>z</sub>* value. The agreement between the experimental data and the calculations is overall very good, and a clear dispersion along *k<sub>z</sub>* is observed, thus verifying the three-dimensional (3D) nature of the bulk bands. The calculated indirect bandgap (between  $\Gamma$  and R points) of 2.9 eV compares well to the experimental value of ~3 eV obtained from optical measurements<sup>7,25</sup> and is lower than the reported 3.7 eV obtained by ARPES<sup>14</sup>. Compared with other theoretical approaches, band gaps calculated by LQSGW tend to be larger than those predicted with LDA and GGA calculations<sup>26</sup>, and similar to the band gaps obtained using hybrid exchange–correlation functionals, such as PBE0<sup>27</sup> and HSE06<sup>28,29</sup>.

From the analysis of the ARPES data, we find the conduction band effective masses in the  $\Gamma$ -X direction to be 0.17 *m<sub>e</sub>*. Our results are in good agreement with the values of 0.20 and 0.22 *m<sub>e</sub>* reported in refs. 11,30, where the authors employed HSE06 and PBE0 hybrid functionals, respectively, as well as with the experimental value of 0.19 *m<sub>e</sub>* reported in ref. 9.

When Ba is substituted with La, the conduction band, which is mainly composed of Sn 5s states (see Supplementary Note 2 for more details), becomes occupied by the donated electrons, turning LBSO into a metal. Previous studies showed that thin films of LBSO could exhibit high conductivity exceeding 10<sup>4</sup> Scm<sup>-1</sup>, and it can be enhanced dramatically at the interface of BSO with another insulator<sup>6</sup>. Indeed, the properties of BSO-based

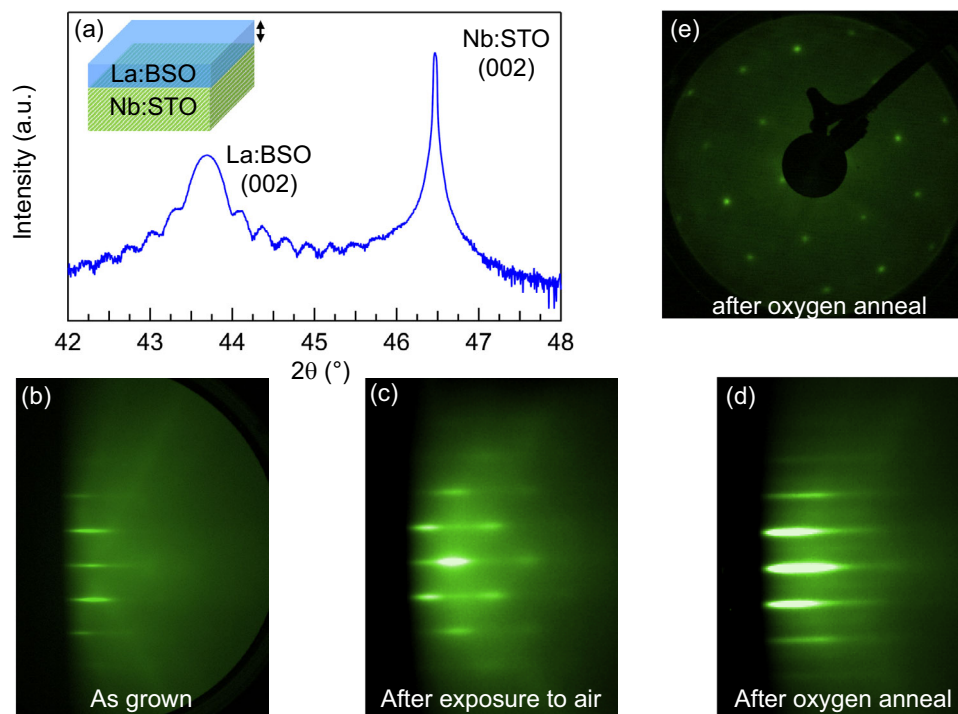


**Fig. 1 X-ray diffraction, reflection high-energy electron diffraction (RHEED), and low-energy electron diffraction (LEED) of La-doped BaSnO<sub>3</sub>.** **a** Angle X-ray diffraction of a 30-nm-thick La-doped BaSnO<sub>3</sub> film grown on (001) oriented Nb-doped SrTiO<sub>3</sub> substrate. RHEED pattern taken along the [100] azimuth after **(b)** growth (in situ at 14 keV), **c** ex situ transfer and exposure to air, and **d** high-temperature oxygen annealing to remove surface contamination. **e** LEED pattern at 147 eV, acquired from the surface after oxygen annealing.

heterostructures strongly depend on the electronic structure of the interface region, which might bear similarities with the BSO film surface. Using vacuum ultraviolet energies for ARPES ensures a short probing depth and thus high sensitivity to the surface electronic structure.

For metallic bulk LBSO, the Fermi surface (FS) is expected to be 3D and isotropic in momentum space, with symmetry inherited from the Sn 5s states, as shown by the red sphere in the sketch of Fig. 2c. Nevertheless, the measured FS lying on the perpendicular  $k_x$ - $k_z$  plane at the Fermi energy (presented in Fig. 2b) shows no clear dispersing bands along  $k_z$ . Occasionally, such behavior can be attributed to the  $k_z$  broadening effect that occurs in ARPES measurements<sup>31</sup>. However, this possibility is unlikely in this case, because the broadening would need to be enormous to stretch the expected small Fermi surface of LBSO to the Brillouin zone boundary. Moreover, the states at  $E_F$  reach the Brillouin zone boundary at the Z point, as indicated by the black squares in Fig. 2b, and their intensity varies with no clear periodicity. The variations in the band's intensity are thus evidently related to the photoemission cross-section, rather than  $k_z$  dispersion. Finally, the values of the Fermi momentum  $k_F$  and bandwidth are similar at different  $k_z$  values (see Fig. 3d). Thus, the measured Fermi surface is cylindrical (sketched in green in Fig. 2c) rather than spherical (shown by the red sphere), indicating the 2D nature of this electronic state.

To obtain more quantitative information about this 2D band, we performed detailed ARPES measurements using a photon energy of 28 eV, which provides the best energy and momentum resolution among all photon energies used in this work. The intensity map at the Fermi energy (Fig. 3b), which is built from several cuts acquired along the direction parallel to  $\Gamma$ -X (see Fig. 3a), confirms the circular shape formed from the electron-like band shown in Fig. 3b, d. According to the Luttinger theorem<sup>32</sup>, the carrier density is proportional to the volume enclosed by the Fermi surface. We extracted the value of the

Fermi momentum,  $k_F$ , by fitting the MDC at  $E_F$  to two Lorentzian curves (Fig. 3d). The measured  $k_F$  of the 2D Fermi surface is found to be smaller than the expected value for bulk ( $k_F \sim 0.067 \text{ \AA}^{-1}$ ), and amounts to a charge carrier density of  $n_{2D}^{ARPES} = 1.2 \times 10^{-2} e^- \text{ per } a^2$  (where  $a$  is the lattice parameter of BSO), which corresponds to  $7 \times 10^{12} e^- \text{ per } \text{cm}^2$ . The carrier density measured by transport for this film<sup>5</sup> is  $n_{3D} = 1.7 \times 10^{20} e^- \text{ per } \text{cm}^3$ . Considering the 2D band to extend over 1–3 unit cells, the bulk carrier density corresponds to a planar density  $n_{2D}$  between  $7 \times 10^{12}$  and  $2 \times 10^{13} e^- \text{ per } \text{cm}^2$ . The similar electron concentrations of the surface state and the bulk suggests homogeneous doping of La across the whole film and imply that the conduction states show an altered dimensionality at the surface. These surface states are reminiscent of Shockley states since they have features of nearly free electron states and occur essentially due to the SnO<sub>2</sub> termination<sup>33</sup>.

Tracking the band dispersion in Fig. 3b, d reveals other unique properties of this 2D state. Keeping  $k_F$  fixed, as determined by Fig. 3c, the experimental spectrum can be well-described by a parabola with the minimum around 0.15 eV and effective mass around  $0.12 m_e$ . The observed value of  $m^*$  is smaller than previously reported values from bulk optical measurements<sup>9</sup> and bulk DFT calculations<sup>8</sup>. Interestingly, the spectra presented in Fig. 3, although with only a moderate background, are rather broad. This broadening can be a sign of many-body interactions, such as electron-phonon coupling. Indeed, it was reported that strong electron-phonon coupling of the conduction electrons with the longitudinal optical LO1, 2, 3 phonon modes is present in BSO<sup>34</sup>. It is also important to note the strong incoherent spectral weight around the  $\Gamma$  point, which is also found in low-doped STO, where it originates from strong electron-phonon coupling<sup>35–37</sup>.

The above results suggest the existence of a 2D state at the LBSO surface, which can be related to the observed 2DEG-like electrical properties in LaInO<sub>3</sub>/BaSnO<sub>3</sub> bilayers<sup>6</sup>. A downward



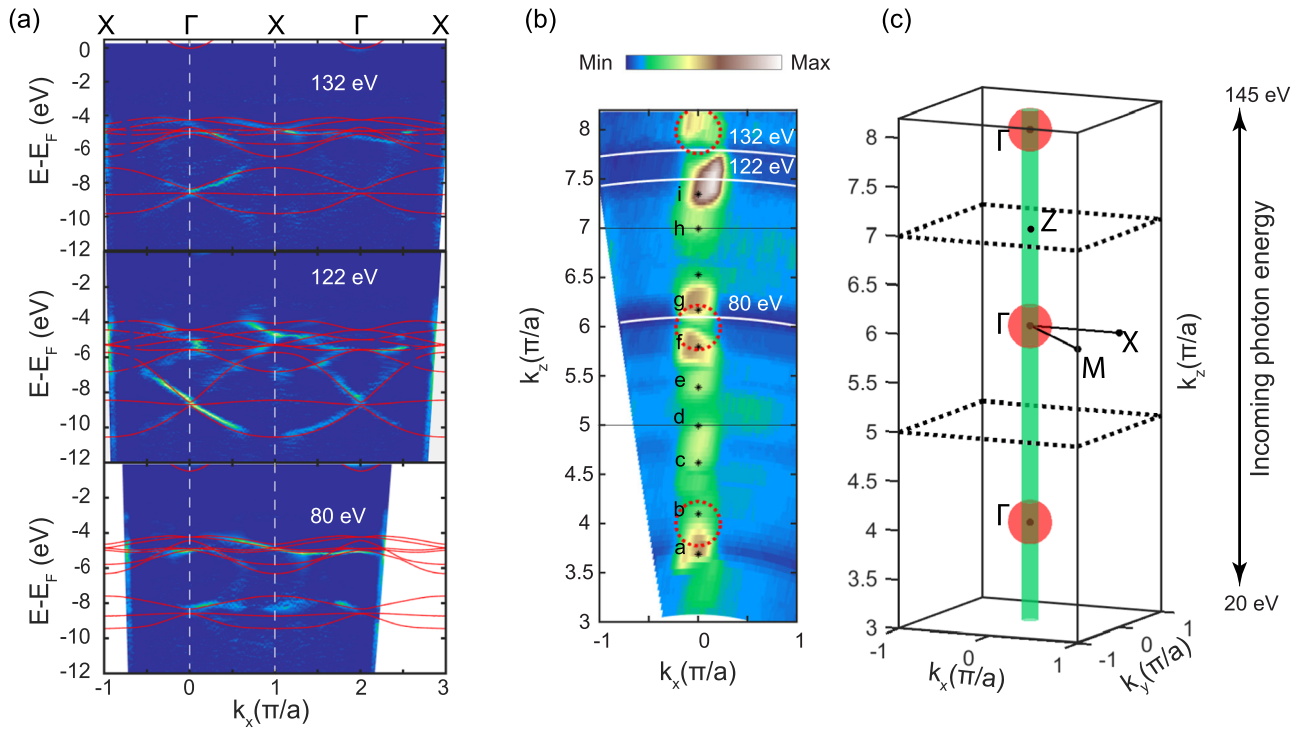


**Fig. 2 Surface and bulk electronic structure of La-doped BaSnO<sub>3</sub>.** **a** Valence band dispersion parallel to  $\Gamma$ -X, acquired with incoming photon energies of 80, 122, and 132 eV, corresponding to different perpendicular momentum  $k_z$  values as indicated by the white curves in **(b)**. The measured band structure is overlaid with the LQSGW band structure calculated for bulk BaSnO<sub>3</sub>. The measured and calculated bands show good agreement, with a clear dispersion along  $k_z$ . **b** Intensity map at the Fermi energy in the plane perpendicular to the sample surface ( $k_x$ - $k_y$ ), measured with incoming photon energies ranging from 20 to 145 eV. No clear periodicity is evident along  $k_z$ . The black squares indicate the Brillouin zone boundaries as inferred by the periodicity of the valence bands shown in panel **(a)**, using the LQSGW calculations as a reference. The red circumferences mark the expected bulk Fermi surface centered at the  $\Gamma$  points **(c)** Sketch illustrating the difference between the measured and calculated Fermi surfaces. The calculated 3D sphere-like Fermi surface with Fermi momentum  $k_F$  based on the nominal doping of the film is shown in red, while the measured 2D cylinder-like Fermi surface with  $k_F$  based on the measurements results is shown in green. ARPES intensity follows the attached color scale bar.

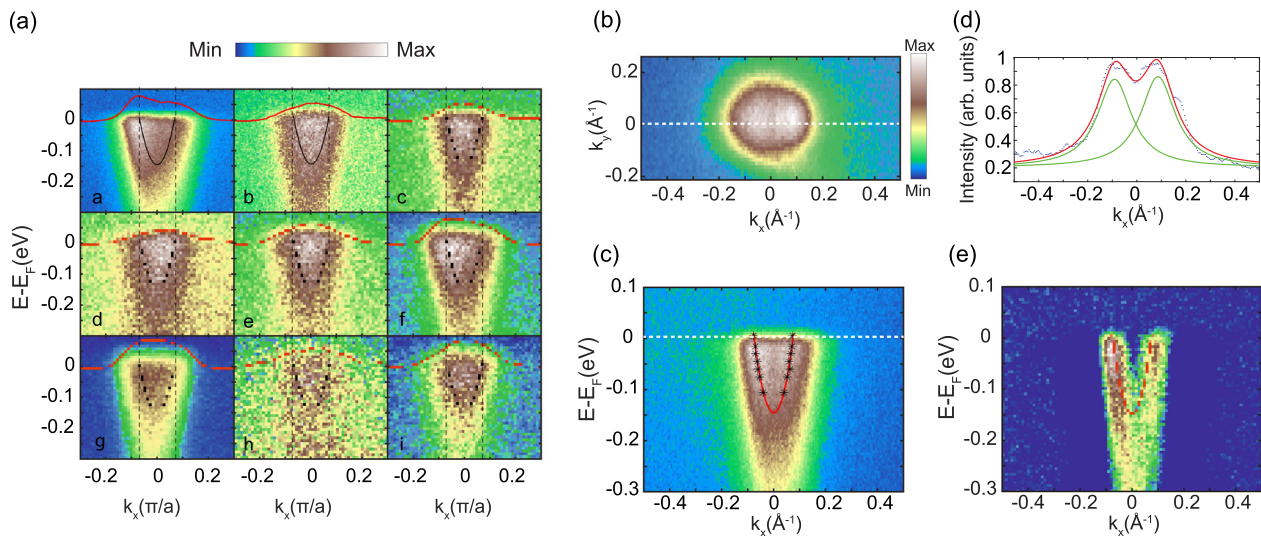


**Fig. 3 Photoemission spectrum near the Fermi energy.** **a** Spectra acquired with different photon energies corresponding to different perpendicular momentum  $k_z$  values, as indicated by black stars in Fig. 2b. For all the acquired bands, the bandwidth and Fermi momentum is similar, as shown by the momentum distribution curves (MDCs) at Fermi energy  $E_F$  (red) and the matched band (black). The vertical dashed lines indicate Fermi momentum  $k_F$ . **b** Intensity map at the Fermi energy assembled from several cuts at different  $k_y$  values. **c** Spectrum image obtained along a cut parallel to the  $\Gamma$ -X direction, as indicated by the dashed white line in **(b)**. The spectra in **(b)** and **(c)** were measured with an incoming photon energy of 28 eV, providing a higher resolution than in previously shown spectra. **d** Momentum distribution curve (MDC) extracted from panel **(c)** at Fermi energy  $E_F$ , and fitted to two Lorentzian profiles to determine the position of Fermi momentum  $k_F$ . **e** Second derivative along the energy axis for the spectrum image in **(c)**, providing an enhanced view of the dispersing band.

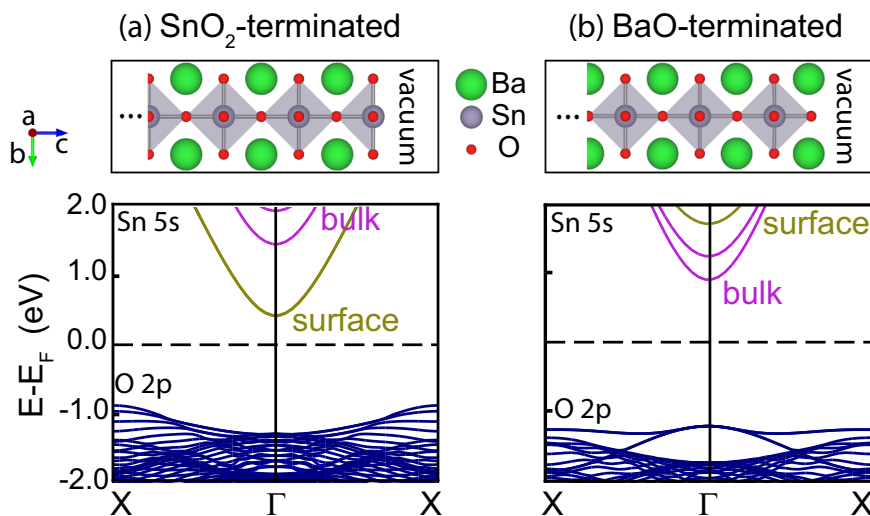


**Fig. 4 Comparison of the calculated electronic structure of BaSnO<sub>3</sub> slab with different terminations.** **a** Optimized SnO<sub>2</sub>-terminated slab structure and corresponding orbital-resolved density functional theory band structure along X-Γ-X. The valence band is dominated by O 2p states, while the conduction band is dominated by Sn 5s states. Bands originating from the surface Sn atoms are highlighted in gold, while bands originating from the Sn atoms in the central layers of the slab, which represent the bulk, are highlighted in pink. **b** Equivalent data for a BaO-terminated slab. The crystal structures were generated with the VESTA software<sup>41</sup>, and the band structures were plotted with PyProcar<sup>42</sup>.

band bending scenario has been proposed to explain the formation of the 2DEG at oxide surfaces, for instance, in the case of STO<sup>21–23</sup>. Indeed, it was experimentally observed that doped BSO films undergo an upward band bending, consequently reducing the conduction band's occupation<sup>12</sup>. Another possible cause of the observed 2D electronic structure can be that breaking translation symmetry on the surface results in a new state whose wave function is localized with different properties than the bulk band<sup>33</sup>. Our ARPES experiments alone cannot disclose the origin of such a state; therefore, we performed the first principle calculations.

To investigate the origin of these 2D states, we simulated  $1 \times 1 \times 8$  BSO (001) slabs with both SnO<sub>2</sub> and BaO terminations. Since LQSGW calculations are computationally too demanding, we performed the electronic structure calculations using the Heyd–Scuseria–Ernzerhof (HSE06)<sup>38</sup> hybrid exchange–correlation functional, which has been shown to provide a good description of the electronic structure and phonon dispersion of bulk BSO<sup>28,29</sup>. The optimized crystal structures, along with their orbital-resolved band structures highlighting the contribution from both surface and bulk Sn 5s orbitals, are shown in Fig. 4a, b for the SnO<sub>2</sub>- and BaO-terminated slabs, respectively. It is interesting to note that the bandgap is, in general, smaller than its bulk counterpart. For the SnO<sub>2</sub>-termination, we found an indirect bandgap of 1.2 eV between the  $\Gamma$  and  $M$  points, while for the BaO-termination it is 2.1 eV. For comparison, we also performed calculations using the PBE<sup>39</sup> exchange–correlation functional for the SnO<sub>2</sub>-terminated slab. Although both calculation methods provided very similar band structures (details about the method employed in our calculations and our experimental procedures are available in Supplementary Note 3), the bandgap with PBE is severely underestimated, leading to a spurious metallic solution that is not observed experimentally (details about the method employed in our calculations and our experimental procedures are available in Supplementary Note 3).

Furthermore, our calculations show that the lowest-lying unoccupied states are mainly derived from Sn 5s orbitals from the surface atoms, while the Sn 5s states from the bulk region of the slab appear around 0.5 eV above. In contrast, for the

BaO-terminated slab, the lowest-lying unoccupied states have predominantly bulk character. The calculated effective masses of both the surface- and bulk-derived state of the SnO<sub>2</sub>-terminated slab, within HSE06, are around  $0.21 m_e$  and  $0.22 m_e$ , respectively. The discrepancy between the effective masses of the 2D state obtained by ARPES ( $0.12 m_e$ ) and calculated with DFT may originate from the in-plane size of the slab and details of the surface structure used in our simulations.

Combining angle-resolved photoemission spectroscopy (ARPES) with ab initio calculations, we revealed the existence of a two-dimensional metallic state at the surface of 1% LBSO thin film, its origin, and characteristics. The comparison between the experimental data and the calculated band structure for BSO slabs indicates that only the SnO<sub>2</sub>-terminated surface hosts this 2D state. The surface state exhibits unique behavior, with an extraordinarily low effective mass of about  $0.12 m_e$ , significantly different from the bulk value. This surface state's particular property, combined with light transparency, warrants BSO a relevant standing among constituent materials of heterostructures for optoelectrical devices.

## Methods

**Sample preparation and characterization.** The LBSO thin films were grown by hybrid molecular beam epitaxy (MBE) at the University of Minnesota on Nb-doped STO (001) substrates. Details of the growth can be found in the report by Prakash et al.<sup>40</sup>. After the growth, the samples were transferred ex situ and loaded into the ARPES system at the SIS beamline of the Swiss Light Source. RHEED patterns were recorded after the ex situ transfer and after each annealing procedure (UHV annealing and annealing at pressure  $1.0 \times 10^{-4}$  mbar of O<sub>2</sub> and temperature 600 °C). All ARPES data presented in the manuscript were obtained from O<sub>2</sub>-annealed samples. The XPS spectra were acquired in the APRES chamber by integrating the angle axis of the spectra images.

## Data availability

The datasets generated during and/or analyzed during this study are available from the corresponding authors upon reasonable request.

Received: 2 April 2022; Accepted: 17 November 2022;

Published online: 07 December 2022

## References

- Zhang, L. et al. Correlated metals as transparent conductors. *Nat. Mater.* **15**, 204+ (2016).
- Luo, X. et al. High carrier mobility in transparent  $\text{Ba}_{1-x}\text{La}_x\text{SnO}_3$  crystals with a wide band gap. *Appl. Phys. Lett.* **100**, 172112 (2012).
- Kim, H. J. et al. High mobility in a stable transparent perovskite oxide. *Appl. Phys. Express* **5**, 061102 (2012).
- Ho, W.-J., Huang, M.-C., Lee, Y.-Y., Hou, Z.-F. & Liao, C.-J. Performance enhancement of ito/oxide/semiconductor mos-structure silicon solar cells with voltage biasing. *Nanoscale Res. Lett.* **9**, 658 (2014).
- Prakash, A. et al. Wide bandgap  $\text{BaSnO}_3$  films with room temperature conductivity exceeding  $10^4 \text{ scm}^{-1}$ . *Nat. Commun.* **8**, 15167 (2017).
- Kim, Y., Kim, Y. M., Shin, J. & Char, K.  $\text{LaInO}_3/\text{BaSnO}_3$  polar interface on  $\text{MgO}$  substrates. *APL Mater.* **6**, 096104 (2018).
- Seo, D. et al. Infrared-optical spectroscopy of transparent conducting perovskite  $(\text{La,Ba})\text{SnO}_3$  thin films. *Appl. Phys. Lett.* **104**, 022102 (2014).
- Lebens-Higgins, Z. et al. Direct observation of electrostatically driven band gap renormalization in a degenerate perovskite transparent conducting oxide. *Phys. Rev. Lett.* **116**, 027602 (2016).
- James Allen, S., Raghavan, S., Schumann, T., Law, K.-M. & Stemmer, S. Conduction band edge effective mass of La-doped  $\text{BaSnO}_3$ . *Appl. Phys. Lett.* **108**, 252107 (2016).
- Niedermeier, C. A. et al. Electron effective mass and mobility limits in degenerate perovskite stannate  $\text{basno}_3$ . *Phys. Rev. B* **95**, 161202 (2017).
- Krishnaswamy, K., Himmetoglu, B., Kang, Y., Janotti, A. & Van de Walle, C. G. First-principles analysis of electron transport in  $\text{basno}_3$ . *Phys. Rev. B* **95**, 205202 (2017).
- Lochocki, E. B., Paik, H., Uchida, M., Schlom, D. G. & Shen, K. M. Controlling surface carrier density by illumination in the transparent conductor La-doped  $\text{BaSnO}_3$ . *Appl. Phys. Lett.* **112**, 181603 (2018).
- Soltani, S. et al.  $\sqrt{2} \times \sqrt{2} \text{R}45^\circ$  surface reconstruction and electronic structure of  $\text{basno}_3$  film. *Phys. Rev. Mater.* **4**, 055003 (2020).
- Joo, B. S. et al. Evidence for indirect band gap in  $\text{BaSnO}_3$  using angle-resolved photoemission spectroscopy. *Curr. Appl. Phys.* **17**, 595–599 (2017). **Oxide Heterostructure Research in Korea.**
- Hwang, H. Y. et al. Emergent phenomena at oxide interfaces. *Nat. Mater.* **11**, 103–113 (2012).
- Wang, Q. et al. Scalable water splitting on particulate photocatalyst sheets with a solar-to-hydrogen energy conversion efficiency exceeding 1%. *Nat. Mater.* **15**, 611–615 (2016).
- Fan, X., Zheng, W., Chen, X. & Singh, D. J. 2degs at perovskite interfaces between  $\text{KTaO}_3$  or  $\text{KNbO}_3$  and stannates. *PLoS ONE* **9**, 1–10 (2014).
- Kim, U., Park, C., Kim, Y. M., Shin, J. & Char, K. Conducting interface states at  $\text{laino}_3/\text{basno}_3$  polar interface controlled by fermi level. *APL Mater.* **4**, 071102 (2016).
- Feng, Z. et al. A two-dimensional electron gas based on a 5s oxide with high room-temperature mobility and strain sensitivity. *Acta Materialia* **204**, 116516 (2021).
- Ohtomo, A. & Hwang, H. Y. A high-mobility electron gas at the  $\text{LaAlO}_3/\text{SrTiO}_3$  heterointerface. *Nature* **427**, 423–426 (2004).
- Meevasana, W. et al. Creation and control of a two-dimensional electron liquid at the bare  $\text{SrTiO}_3$  surface. *Nat. Mater.* **10**, 114 (2011).
- Santander-Syro, A. F. et al. Two-dimensional electron gas with universal subbands at the surface of  $\text{SrTiO}_3$ . *Nature* **469**, 189 (2011).
- Plumb, N. C. et al. Mixed dimensionality of confined conducting electrons in the surface region of  $\text{SrTiO}_3$ . *Phys. Rev. Lett.* **113**, 086801 (2014).
- Zhang, P. et al. A precise method for visualizing dispersive features in image plots. *Rev. Sci. Instrumen.* **82**, 043712 (2011).
- Liu, Q. et al. Composition dependent metal-semiconductor transition in transparent and conductive la-doped  $\text{basno}_3$  epitaxial films. *Appl. Phys. Lett.* **101**, 241901 (2012).
- Moreira, E. et al. Structural and electronic properties of  $\text{srxba1axsno}_3$  from first principles calculations. *J. Solid State Chemistry* **187**, 186–194 (2012).
- Scanlon, D. O. Defect engineering of  $\text{BaSnO}_3$  for high-performance transparent conducting oxide applications. *Phys. Rev. B* **87**, 161201 (2013).
- Kim, B. G., Jo, J. & Cheong, S. Hybrid functional calculation of electronic and phonon structure of  $\text{basno}_3$ . *J. Solid State Chemistry* **197**, 134–138 (2013).
- Liu, H.-R., Yang, J.-H., Xiang, H. J., Gong, X. G. & Wei, S.-H. Origin of the superior conductivity of perovskite  $\text{ba}(\text{sr})\text{sno}_3$ . *Appl. Phys. Lett.* **102**, 112109 (2013).
- Scanlon, D. O. Defect engineering of  $\text{basno}_3$  for high-performance transparent conducting oxide applications. *Phys. Rev. B* **87**, 161201 (2013).
- Lou, R. et al. Experimental observation of bulk nodal lines and electronic surface states in  $\text{ZrB}_2$ . *npj Quant. Mater.* **3**, 43 (2018).
- Luttinger, J. M. Fermi surface and some simple equilibrium properties of a system of interacting fermions. *Phys. Rev.* **119**, 1153–1163 (1960).
- Shockley, W. On the surface states associated with a periodic potential. *Phys. Rev.* **56**, 317–323 (1939).
- Niedermeier, A. et al. Electron effective mass and mobility limits in degenerate perovskite stannate  $\text{basno}_3$ . *Phys. Rev. B* **95** <https://doi.org/10.1103/PhysRevB.95.161202> (2017).
- Chen, C., Avila, J., Frantzeskakis, E., Levy, A. & Asensio, M. C. Observation of a two-dimensional liquid of frohlich polarons at the bare  $\text{SrTiO}_3$  surface. *Nat. Commun.* **6**, 1–8 (2015).
- Wang, Z. et al. Tailoring the nature and strength of electron-phonon interactions in the  $\text{srtio}_3(001)$  2d electron liquid. *Nat. Mater.* **15**, 835+ (2016).
- Cancellieri, C. et al. Polaronic metal state at the  $\text{LaAlO}_3/\text{SrTiO}_3$  interface. *Nat. Commun.* **7**, 1–8 (2016).
- Heyd, J., Scuseria, G. E. & Ernzerhof, M. Hybrid functionals based on a screened coulomb potential. *J. Chem. Phys.* **118**, 8207–8215 (2003).
- Perdew, J. P., Burke, K. & Ernzerhof, M. Generalized gradient approximation made simple. *Phys. Rev. Lett.* **77**, 3865–3868 (1996).
- Prakash, A. et al. Hybrid molecular beam epitaxy for the growth of stoichiometric  $\text{BaSnO}_3$ . *J. Vacuum Sci. Technol. A* **33**, 060608 (2015).
- Momma, K. & Izumi, F. VESTA3 for three-dimensional visualization of crystal, volumetric and morphology data. *J. Appl. Crystallography* **44**, 1272–1276 (2011).
- Herath, U. et al. Pyprocar: a python library for electronic structure pre/post-processing. *Computer Phys. Commun.* **251**, 107080 (2020).

## Acknowledgements

M.N. was supported by the ISRAEL SCIENCE FOUNDATION (grant No. 2509/20). The work at Swiss Light Source was supported by SNSF Research Grant 200021\_182695. The work at UMN was supported by the Air Force Office of Scientific Research (AFOSR) through Grant No. FA9550-21-1-0025. Parts of this work were carried out at the Minnesota Nano Center and Characterization Facility, the University of Minnesota, which receives support from NSF through the MRSEC program DMR-2011401. W.H.B. and H.M.C. acknowledge the Pró-Reitoria de Pesquisa of Universidade Federal de Minas Gerais, CNPq, and the National Laboratory for Scientific Computing (LNCC/MCTI, Brazil) for providing HPC resources of the SDumont supercomputer, <http://sdumont.lncc.br>. M.S. acknowledges support from the Swiss National Science Foundation (grant no. 200021-188413).

## Author contributions

M.R. and J.B. conceived the project. A.P. and B.J. grew and characterized the samples. M.N., E.B.G., and M.R. with the help of A.P., N.C.P., and M.S. performed the ARPES measurements and analyzed the data. H.M.C. and W.H.B. carried out the theoretical calculations. M.N., E.B.G., and M.R. wrote the manuscript with input from all authors.

## Competing interests

The authors declare no competing interests.

## Additional information

**Supplementary information** The online version contains supplementary material available at <https://doi.org/10.1038/s42005-022-01091-y>.

**Correspondence** and requests for materials should be addressed to Muntaser Naamneh, Bharat Jalan or Milan Radović.

**Peer review information** *Communications Physics* thanks the anonymous reviewers for their contribution to the peer review of this work.

**Reprints and permission information** is available at <http://www.nature.com/reprints>

**Publisher's note** Springer Nature remains neutral with regard to jurisdictional claims in published maps and institutional affiliations.



**Open Access** This article is licensed under a Creative Commons Attribution 4.0 International License, which permits use, sharing, adaptation, distribution and reproduction in any medium or format, as long as you give appropriate credit to the original author(s) and the source, provide a link to the Creative Commons license, and indicate if changes were made. The images or other third party material in this article are included in the article's Creative Commons license, unless indicated otherwise in a credit line to the material. If material is not included in the article's Creative Commons license and your intended use is not permitted by statutory regulation or exceeds the permitted use, you will need to obtain permission directly from the copyright holder. To view a copy of this license, visit <http://creativecommons.org/licenses/by/4.0/>.

© The Author(s) 2022